

## Multiphase alkaline water electrolysis simulations

### The need for a solid pressure model to explain experimental bubble overpotentials

van der Does, W. L.; Valle, N.; Haverkort, J. W.

**DOI**

[10.1016/j.ijhydene.2024.12.252](https://doi.org/10.1016/j.ijhydene.2024.12.252)

**Publication date**

2025

**Document Version**

Final published version

**Published in**

International Journal of Hydrogen Energy

**Citation (APA)**

van der Does, W. L., Valle, N., & Haverkort, J. W. (2025). Multiphase alkaline water electrolysis simulations: The need for a solid pressure model to explain experimental bubble overpotentials. *International Journal of Hydrogen Energy*, 102, 295-303. <https://doi.org/10.1016/j.ijhydene.2024.12.252>

**Important note**

To cite this publication, please use the final published version (if applicable). Please check the document version above.

**Copyright**

Other than for strictly personal use, it is not permitted to download, forward or distribute the text or part of it, without the consent of the author(s) and/or copyright holder(s), unless the work is under an open content license such as Creative Commons.

**Takedown policy**

Please contact us and provide details if you believe this document breaches copyrights. We will remove access to the work immediately and investigate your claim.



# Multiphase alkaline water electrolysis simulations: The need for a solid pressure model to explain experimental bubble overpotentials

W.L. van der Does<sup>\*</sup>, N. Valle, J.W. Haverkort

*Delft University of Technology, Process & Energy Department, Leeghwaterstraat 39, Delft, 2628 CB, The Netherlands*

## ARTICLE INFO

### Keywords:

Alkaline water electrolysis  
Zero-gap electrode configuration  
Solid pressure  
Bubble resistance  
Multiphase flow  
Mixture model

## ABSTRACT

As current densities in alkaline water electrolyzers increase, the resistive losses become increasingly important due to the locally high gas fraction around the electrodes, even in zero-gap configurations. Nonetheless, quantitative measurement of the distribution of these high gas fractions is difficult. Consequently, a numerical approach is useful to assess the impact of bubbles on electrolysis. However, models that couple current density and gas fraction distributions in a non-trivial geometry are currently lacking. We show that typically used models in the literature predict unrealistically high gas fractions in electrode-resolved simulations. To improve this, we added to the mixture model equations a solid pressure model similar to that used in simulations of dense granular flows. With the addition of this model, two-dimensional simulations of a lab-scale electrolysis cell accurately reproduce previously reported experimental results. This allows, for the first time, to predict local overpotentials influenced by the bubble distribution, opening the way towards computational optimisation of the electrode geometry.

## 1. Introduction

Industrial electrolyzers are usually operated at high current densities to be economically attractive [1]. Under these conditions, ohmic losses become increasingly important. This is particularly true for gas-evolving electrodes, for example in alkaline water electrolyzers, where gas bubbles generated at the electrodes further add to the ohmic resistance. To minimise the ohmic resistance, a so-called zero-gap configuration is often employed [2–5]. In this case, the electrodes are pressed directly onto a porous diaphragm which separates the hydrogen-evolving cathode and the oxygen-evolving anode. This minimises the distance between the electrodes and, by using electrodes with large perforations, pores, or wire meshes, the bubbles can be directed outside of the electrode-diaphragm assembly [6–8]. While this is expected to minimise the ohmic losses, gas bubbles in and around the open spaces of the electrode are still found to contribute significantly to the resistance of the electrolyser [9]. Additionally, gas cross-over across the diaphragm is known to occur in zero-gap alkaline water electrolysis, possibly leading to severe safety risks [10,11]. It is therefore of great interest to understand the behaviour and transport of electrogenerated bubbles. In this work, we propose a computational approach to model the transport of gas bubbles near a zero-gap electrode configuration in an alkaline water electrolyser.

Various experimental studies concern the development of bubble plumes along gas-evolving electrodes, and their effects on the vertical

distribution of current in alkaline water electrolysis [12–21]. However, the vast majority of these studies use a traditional electrolyser configuration, where the bubbles are released into the space between the electrodes or between the electrodes and the membrane. By contrast, in a zero-gap configuration, the bubbles are directed to the outside of the electrode assembly. As a result, the impact of the vertical gas distribution on the current distribution is reduced. However, various studies indicate that small geometric features of the electrodes can be responsible for big difference in cell voltage and electrochemical performance [22,23]. Since during electrolysis large amounts of small bubbles are generated that obscure the view of the electrodes, optical analysis of the gas fraction distribution extremely difficult. Consequently, a numerical approach is proposed here to provide further insight into the effect of bubbles on the current distribution.

Several computational works have previously simulated the 2-D current distribution in a zero-gap configuration for gas-evolving electrodes [24–27]. A similar numerical approach was recently used to further investigate the effect of gas bubbles near a zero-gap electrode [4]. These studies show that the presence of bubbles inside the electrode assembly can significantly increase the ohmic losses, and can help explain the voltage losses found in experimental studies. However, these previous studies did not include multiphase flow, and instead assumed a homogeneous gas fraction. While this assumption significantly

<sup>\*</sup> Corresponding author.

E-mail address: [W.L.vanderDoes@tudelft.nl](mailto:W.L.vanderDoes@tudelft.nl) (W.L. van der Does).

**Nomenclature**

$\hat{z}$	Unit vector in the vertical z-direction
$\mathbf{n}$	Normal vector
$\mathbf{U}$	Superficial velocity [m/s]
$\mathbf{u}$	Velocity [m/s]
$\mathbf{u}_{\text{Hd}}$	Hydrodynamic diffusion slip velocity [m/s]
$\mathbf{u}_{\text{Sd}}$	Shear diffusion slip velocity [m/s]
$\mathbf{u}_{\text{Sp}}$	Solid pressure slip velocity [m/s]
$\mathbf{u}_{\text{St}}$	Stokes slip velocity [m/s]
$\mathbf{u}_s$	Slip velocity [m/s]
$\mathcal{V}_m$	Molar volume [m <sup>3</sup> /mol]
$C$	Modulus of elasticity function parameter
$D$	Hydrodynamic diffusivity [m <sup>2</sup> /s]
$d_b$	Bubble diameter [m]
$E$	Potential [V]
$G(\epsilon)$	Solid pressure modulus of elasticity function
$i_n$	Normal current density [A/m <sup>2</sup> ]
$j$	Current density [A/m <sup>2</sup> ]
$j_*$	Exchange current density [A/m <sup>2</sup> ]
$j_{\perp}$	Local current density on electrode surface [A/m <sup>2</sup> ]
$K$	Stress tensor [Pa]
$n$	Number of electrons per molecule
$p$	Pressure [Pa]
$p_s$	Solid pressure [Pa]
$S_{e/d}$	1-dimensional electrode/diaphragm surface [m]
$T$	Temperature
$U_g$	Volumetric gas flux at the electrode [m/s]
$w_{\text{St}}$	Terminal rise velocity [m/s]
$x$	Horizontal coordinate [m]
$z$	Vertical coordinate [m]
<b>Constants</b>	
$F$	Faraday's constant 96485.332... [C/mol]
$R$	Gas constant 8.31446... [J/mol/K]
<b>Greek variables</b>	
$\alpha$	Charge transfer coefficient
$\gamma_{0/1/2}$	Solid pressure parameter in J&J model
$\kappa$	Effective electrolyte conductivity [S/m]
$\kappa_0$	Electrolyte conductivity [S/m]
$\mu$	Dynamic viscosity [Pa/s]
$\Phi$	Electrode potential [V]
$\phi$	Electrolyte potential [V]
$\rho$	Density [kg/m <sup>3</sup> ]
$\epsilon$	Void fraction
$\epsilon^*$	Modulus of elasticity function parameter
$\epsilon_{\text{max}}$	Maximal void fraction in J&J solid pressure
$\epsilon_{\text{min}}$	Minimal void fraction in J&J solid pressure
<b>Subscripts</b>	
a	Anode
cell	cell
c	Cathode

eq	Equilibrium conditions
g	Gas phase
in	Inlet
l	Liquid phase
m	Mixture
out	Outlet

**Table 1**

Previous multiphase CFD works on alkaline water electrolyzers using laminar flow models.

Researchers	Bubble dispersion force model	Other force models, e.g. lift	Electrochemistry coupling	Electrode shape resolved
Dahlkild [28]	✓	✗	✓	✗
Wedin and Dahlkild [37]	✓	✓	✓	✗
Mandin et al. [46]	✓	✗	✓	✗
Aldas et al. [32]	✗	✗	✓	✗
Jupudi et al. [29]	✓	✗	✓	✗
Alexiadis et al. [47]	✓	✗	✗	✗
Hreiz et al. [48]	✗	✗	✗	✗
Schillings et al. [38]	✓	✓	✗	✗
Schillings et al. [39]	✓	✓	✗	✗
Bideau et al. [41]	✓	✓	✗	✗
Hess et al. [49]	✗	✗	✓	✗
Duan et al. [36]	✓	✓	✓	✗
This work	✓	✗	✓	✓

reduces the complexity of the simulations, experimental observations indicate that the size and shape of the electrodes can have strong effects on the bubble behaviour [14,15] and ohmic losses [22,23]. Consequently, there is a need to better understand the bubble behaviour around electrodes. Various multiphase flow simulations of alkaline water electrolysis exist in the literature. The vast majority of these studies consider the evolution of a bubble plume along a flat vertical electrode. Some include the effect of bubbles on the current distribution [28–36] while others assume a constant current density [37–44]. An attempt to categorise most of these studies is given in Table 1. We restrict ourselves here to alkaline water electrolysis with laminar flow.

Due to the high costs associated with computational methods that attempt to resolve the gas-liquid interface for every bubble, most studies employ either the two-fluid or the mixture model. However, this approach requires the use of closure models to capture the sub-scale flow features. In particular, it is found that some form of an additional bubble dispersion mechanism is required to accurately predict the widening of a bubble plume along a vertical gas-evolving electrode [28, 38,41,42,45]. A notable exception is the work by Schillings et al. [39], who use a 4-way coupled Eulerian-Lagrangian approach which includes a bubble collision event model able to predict plume widening without the need for empirical closure models.

Nonetheless, all multiphase flow studies mentioned in Table 1 concerned either a flat-plate electrode geometry or in some cases a porous electrode region for highly porous metal foam electrodes. To our best knowledge, no existing studies have attempted to simultaneously resolve the multiphase flow and bubble transport around the resolved structure of the electrodes in zero-gap alkaline water electrolysis. Here, we propose a model that couples the distribution of gas fraction and current in a physical way.

In the holes of zero-gap electrodes, there will be less flow than on vertical surfaces so bubble-bubble interactions are expected to dominate gas removal. While average gas volume fractions have been studied and quantified in the bulk flow of alkaline water electrolyzers [14, 20], no direct measurements of the local gas fraction distribution inside the perforations of the electrodes exist. However, visual observations from behind the electrode [9,50] and through the membrane [51–56] suggest that inside these holes the maximum random bubble packing fraction is approached at high current densities. In addition, in concentrated electrolytes, bubbles are known to show coalescence inhibition [14,57,58]. This allows us, as a first approximation, to use equations similar to those used for modeling solid particles.

The purpose of this paper is to include additional bubble dispersion through a solid-pressure model similar to that used for granular flows, in the holes of the electrodes in a zero-gap configuration. This represents a significant progress from previous studies and constitutes a novel approach to describing bubble transport in confined regions.

The rest of the paper is organised as follows: Section 2 introduces the model geometry and numerical approach used to describe the multiphase flow and electrochemistry, along with the considered closure models. Section 3 shows simulation results for the gas fraction distribution, velocity profiles, and bubble-induced voltage losses for the different solid-pressure models. Section 4 then further investigates the various voltage losses in the system and validates them against experimental results from Haverkort and Rajaei [9].

## 2. Methods

### 2.1. Multiphase flow

The two-phase hydrodynamics are described using the mixture model for laminar, incompressible flow [28,59]. The mixture model is based on an Eulerian framework and treats each phase as an interpenetrating continuum. A condition for the mixture model validity is for the continuous and dispersed phase to be in dynamic equilibrium. This means that there is no relative acceleration between the two phases and the sum of forces on the bubbles is zero [60]. This is a reasonable approximation for the small bubbles that arise in electrolysis. We further assume that the gas bubbles are spherical, that the bubbles do not coalesce [14,57,58], and that the zero-gap electrode assembly can be reasonably described with the two-dimensional geometry shown in Fig. 1. Due to the large amount of bubbles, it is computationally unfeasible to capture all features of this kind of flow. To address this, the mixture model uses the gas fraction  $\epsilon$  to represent the amount of bubbles present in each computational cell. The volume-averaged velocity of the mixture  $\mathbf{U}$  is then given by  $\mathbf{U} = (1 - \epsilon)\mathbf{u}_l + \epsilon\mathbf{u}_g$ , where  $\mathbf{u}_l$  and  $\mathbf{u}_g$  denote the liquid and gas velocities. Since the gas density is negligible compared to the liquid density  $\rho_l$ , the mixture density is  $\rho_m = (1 - \epsilon)\rho_l$  and the mass-averaged mixture velocity  $\mathbf{U}_m$  is equal to the superficial liquid velocity  $\mathbf{U}_l = \rho_l(1 - \epsilon)\mathbf{u}_l$ . The continuity equation for the mixture in a steady state is

$$\nabla \cdot \mathbf{U}_m = 0 \quad (1)$$

The mixture model relies on solving a single momentum equation which represents the transport of the mixture of liquid and gas as a whole. The momentum equation for the mixture in a steady-state is

$$\rho_m \mathbf{u}_l \cdot \nabla \mathbf{u}_l = -\nabla p + \nabla \cdot \mathbf{K} - \rho_m g \hat{z} \quad (2)$$

where  $\mu_m = \frac{\mu_l}{1-\epsilon}$  is the mixture viscosity [61], and  $\mathbf{K} = \mu_m (\nabla \mathbf{U} + (\nabla \mathbf{U})^T)$  is the mixture viscous stress tensor.

We model the actual velocities of the liquid and gas phases in terms of the slip velocity  $\mathbf{u}_s = \mathbf{u}_g - \mathbf{u}_l$ , which represents the difference between the gas and liquid velocities, and the slip flux or drift flux  $\mathbf{U}_s = \epsilon (\mathbf{u}_g - \mathbf{U}) = \epsilon (1 - \epsilon) \mathbf{u}_s$ , after which we obtain from  $\nabla \cdot (\epsilon \mathbf{u}_g) = 0$  the gas continuity equation:

$$\mathbf{U} \cdot \nabla \epsilon + \nabla \cdot \mathbf{U}_s = 0 \quad (3)$$

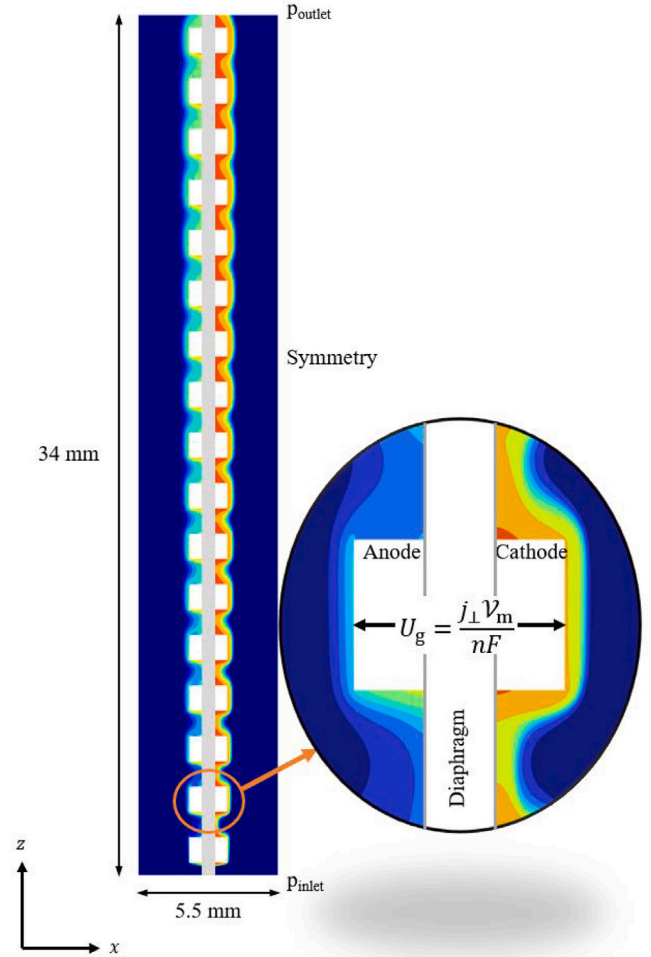


Fig. 1. Representation of the two-dimensional simulation geometry, coordinates and boundary conditions. See Eq. (16b) for the expressions used for the inlet and outlet pressures  $p_{in}$  and  $p_{out}$  and Eq. (17) for the expression used for the symmetry boundary condition. The symmetry boundary condition prescribes vanishing stresses in the  $z$  direction. The grayed domain in the centre represents the diaphragm, and the white regions bordering this represent the two electrodes. Inside the diaphragm, the fluid flow is not solved for, and only current and potential distributions are simulated. At the electrodes bubbles evolve, which is represented in the gas fraction  $\epsilon$  and by the coloured surface in the figure. (For interpretation of the references to colour in this figure legend, the reader is referred to the web version of this article.)

The actual sub-grid model for  $\mathbf{u}_s$  is the combination of different slip velocities, each modeling a different slip mechanism:

$$\mathbf{u}_s = \mathbf{u}_{St} + \mathbf{u}_{Hd} + \mathbf{u}_{Sd} + \mathbf{u}_{Sp} \quad (4)$$

where  $\mathbf{u}_{St}$  is Stokes' rise velocity,  $\mathbf{u}_{Hd}$  is hydrodynamic dispersion,  $\mathbf{u}_{Sd}$  is shear diffusion and  $\mathbf{u}_{Sp}$  is solid pressure.

In this study, we use an adapted version of the slip velocity closure models presented by Dahlkild [28]. The formulation for these slip velocities arise from assuming that all forces acting on the bubbles are in equilibrium with the drag force. Here, we assume that the drag force can be described by Stokes' drag, which is generally valid for electrolytic bubbles smaller than  $100 \mu\text{m}$  [62].

$$\mathbf{u}_{St} = f(\epsilon) w_{St} \hat{z} \quad (5)$$

$$\mathbf{u}_{Hd} = -f(\epsilon) \frac{d_b w_{St}}{2} \frac{\nabla \epsilon}{\epsilon} \quad (6)$$

$$\mathbf{u}_{Sd} = -\frac{d_b^2}{4} \left| \frac{\partial w}{\partial x} + \frac{\partial u}{\partial z} \right| \frac{\epsilon(1 + 0.5e^{8.8\epsilon})}{3(1 - \epsilon)} \nabla \epsilon \quad (7)$$

The difference in density between the bubbles and the liquid gives a buoyancy-induced rise velocity  $\mathbf{u}_{St}$ , where  $w_{St} = \frac{\rho_l g d_b^2}{18\mu_l}$  is the terminal

**Table 2**

The various values for the parameters in Eq. (9) from literature.

Author	C	$\epsilon^*$
Gidaspow & Ettadieh 1983 [71]	20.17	0.38
Ettadieh 1984 [72]	24.09	0.37
Shih 1987 [73]	22.48	0.20
Gidaspow 1989 [74]	24.18	0.14

rise velocity of a single bubble due to buoyancy.

The second slip velocity  $\mathbf{u}_{\text{Hd}}$  is the hydrodynamic self-diffusion. This term is due to collision-like interactions between bubbles, and is based on observations for suspended particles [63]. In general, the dispersion may have to be split in a direction parallel and normal to the bubble motion. However, in the absence of experimental validation of this assumption we opt for simplicity and consider isotropic dispersion. Here  $f(\epsilon) = (1 - \epsilon)^n$  is a hindrance function for a swarm of rising bubbles, in which a high concentration of bubbles results in slower velocities relative to the liquid. We use  $n = 4$  which results in a hindrance function similar to what was used previously [38,64].

The third slip velocity component  $\mathbf{u}_{\text{sd}}$  represents shear diffusion, where increased bubble-bubble interactions in a sheared flow result in more bubble dispersion [65].

In addition, at high void fractions, inter-particle collisions will become more important, similar to the particle interactions in dense granular flows, which result into an additional slip velocity to account for this mechanism. These interactions result in increased dispersion of the particles, which is often described with sub-scale models like the so-called solid pressure  $p_s$  [66,67], which leads to the inclusion of solid pressure slip velocity  $\mathbf{u}_{\text{sp}}$ . In alkaline water electrolysis, the bubbles behave like rigid spheres due to their small diameter and since coalescence is largely inhibited due to the presence of strong electrolytes [14,57,58]. From this behaviour, an analogy between rigid, spherical bubbles and solid particles is made, and we propose the use of solid pressure to describe the strongly increased bubble dispersion rates at high gas fractions.

Several models describing solid pressure exists in the literature, among them:

$$\nabla p_s = \begin{cases} \gamma_0 \rho g d_b \nabla \left( \frac{(\epsilon - \epsilon_{\min})^{\gamma_1}}{(\epsilon_{\max} - \epsilon)^{\gamma_2}} \right) & \text{Jackson \& Johnson} \\ G(\epsilon) \nabla \epsilon & \text{Modulus of Elasticity} \end{cases} \quad (8)$$

where the modulus of elasticity  $G(\epsilon)$  is defined as [68]

$$G(\epsilon) = e^{-C(\epsilon^* - \epsilon)} \quad (9)$$

This is then translated [69] to the slip velocity component  $\mathbf{u}_{\text{sp}}$

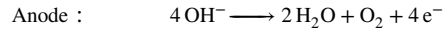
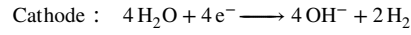
$$\mathbf{u}_{\text{sp}} = -\frac{d_b^2 \nabla p_s}{18 \mu \epsilon} \quad (10)$$

Many different parameters for these solid pressure models exist in literature. For the Jackson & Johnson solid pressure model in Eq. (8), we use  $\gamma_0 = 0.002$ ,  $\gamma_1 = 2$ ,  $\gamma_2 = 5$ ,  $\epsilon_{\min} = 0$ , and  $\epsilon_{\max} = 0.65$  [70]. This represents a combination of the parameters originally proposed by Jackson & Johnson, and the maximum gas fraction from experimental results by Coenen & Janssen for hydrogen bubbles in alkaline water electrolysis [20]. For the modulus of elasticity approach, four sets of parameters are given in Table 2.

Note that inserting Eq. (6) into Eq. (3) gives an advection-diffusion equation with a diffusion coefficient given by  $(1 - \epsilon)^{n+1} d_b w_{\text{St}}/2$ . Note also the similarities between the solid-pressure slip velocity of Eq. (10) and hydrodynamic dispersion of Eq. (6). Therefore, solid pressure can be considered to be another dispersion mechanism, which increases and diverges as the maximum gas fraction  $\epsilon_{\max}$  is approached.

## 2.2. Electrochemistry coupling

The liquid phase consists of a concentrated solution of potassium hydroxide salt (KOH) dissolved in water. In the resulting alkaline solution, the hydrogen and oxygen evolution reactions are given by, respectively



The hydroxide ions produced at the cathode and consumed at the anode are the charge carriers in the electrolyte between the electrodes. An excellent approximation is to assume the concentrations of  $\text{K}^+$  and  $\text{OH}^-$  to be equal to give electroneutrality [75]. At high electrolyte concentrations and sufficient mixing, the electrolyte concentration can be take to be approximately homogeneous and the current density can then be approximately described by Ohm's law:

$$\mathbf{i} = -\kappa \nabla \phi \quad (11)$$

where  $\mathbf{i}$  is the ionic current density,  $\kappa$  is the electrolyte conductivity, and  $\phi$  is the electrostatic potential in the electrolyte. The effective conductivity of the electrolyte is reduced in the presence of bubbles. A reasonably accurate description of the effect of gas fraction on the effective conductivity of the electrolyte is given by Bruggeman's equation [75]

$$\kappa = \kappa_0 (1 - \epsilon)^{3/2} \quad (12)$$

where  $\kappa_0$  is the intrinsic conductivity of the electrolyte. The conductivity of the diaphragm is given by  $\kappa = \kappa_0 \epsilon / \tau^2$  with  $\epsilon / \tau^2 = 0.35$  the ratio of porosity and tortuosity squared [75], experimentally determined in [76]. The reaction kinetics at the electrode surface are described by the concentration-independent Butler-Volmer equation

$$j_{\perp} = j_* \left( e^{\frac{\alpha F \eta}{RT}} - e^{-\frac{(1-\alpha) F \eta}{RT}} \right) \quad (13)$$

where  $j_{\perp}$  is the local current density at the electrode surface,  $j_*$  is the exchange current density,  $\alpha$  is the charge transfer coefficient, and  $\eta$  is the activation overpotential, which defined as  $\eta = (E - \phi) - (E - \phi)_{\text{eq}}$  with the electrode potential  $E$  and a subscript eq denoting equilibrium values at  $j_{\perp} = 0$  [75].

Since the electrolyte potential and activation overpotential vary locally as a result of the current distribution model, a current density weighted average is used to determine and compare the different overpotentials along the electrodes and diaphragm:

$$\langle \eta \rangle \equiv \frac{\int_{S_e} j_{\perp} \eta \, dS_e}{j S_e} \quad (14a)$$

$$\langle \phi_e \rangle \equiv \frac{\int_{S_e} j_{\perp} \phi \, dS_e}{j S_e} \quad (14b)$$

$$\langle \phi_d \rangle \equiv \frac{\int_{S_d} i_n \phi \, dS_d}{j S_d} \quad (14c)$$

with  $S_e$  and  $S_d$  the areas of the electrode and the diaphragm, respectively, and  $i_n$  the current density normal to the diaphragm surface. The total ohmic losses are then obtained from the difference in potential between the cathodic and the anodic sides of the electrodes or the diaphragm.

## 2.3. Boundary conditions and model parameters

At the bottom inlet and top outlet, we use pressure boundary conditions

$$(-p\mathbf{I} + \mathbf{K}) \cdot \mathbf{n} = -p_{\text{in/out}} \mathbf{n} \quad (15)$$

with a mixed hydrostatic and local Bernoulli boundary condition at the inlet and a fixed prescribed pressure at the outlet

$$p_{\text{in}}(x) = -\frac{1}{2} \rho_1 (W(x)(1 - \epsilon))^2 \quad (16a)$$

**Table 3**

Simulation parameters taken from [9]. These parameters have been used in the computational simulations, unless stated otherwise.

Temperature	$T$	300 K
Density [80]	$\rho_l$	1260 kg/m <sup>3</sup>
Viscosity [80]	$\mu_l$	1.9 mPa s
Bubble diameter H <sub>2</sub>	$d_{b,H_2}$	40 $\mu$ m
Bubble diameter O <sub>2</sub>	$d_{b,O_2}$	80 $\mu$ m
Anode exchange current density	$j_{*,a}$	200 A/m <sup>2</sup>
Cathode exchange current density	$j_{*,c}$	800 A/m <sup>2</sup>
Anode charge transfer coefficient	$\alpha_a$	0.65
Cathode charge transfer coefficient	$\alpha_c$	0.5
Electrolyte conductivity	$\kappa_0$	65.4 S m <sup>-1</sup>
Equilibrium potential	$E_0$	1.38 V
Areal electronic resistance	$AR$	17 $\mu\Omega$ m <sup>2</sup>
Jackson & Johnson model parameters	$\gamma_0$	0.002
	$\gamma_1, \gamma_2$	2, 5
	$\epsilon_{\min}, \epsilon_{\max}$	0, 0.65

$$p_{\text{out}}(x) = -\rho_l g H + \begin{cases} -\frac{1}{2} \rho_l (W(x)(1-\epsilon))^2 & W(x) < 0 \\ 0 & W(x) \geq 0 \end{cases} \quad (16b)$$

The mixed hydrostatic and local Bernoulli pressure boundary condition best reproduced the return flow intensity on the inlet and outlet boundaries observed in natural convection experiments Brangeon et al. [77], Sun et al. [78], Desrayaud et al. [79]. In Eq. (16b)  $W$  is the upward component of the volume-averaged mixture velocity. At the outlet, the external dispersed phase concentration  $\epsilon_{\text{out}} = 0$  so that any potential backflow of electrolyte does not re-introduce additional gas into the domain. At the outwards-facing boundaries, symmetry boundary conditions, of no slip and zero tangential viscous stress, are applied:

$$\mathbf{U} \cdot \mathbf{n} = 0 \quad (17a)$$

$$\mathbf{t}^T \mathbf{K} \mathbf{n} = 0 \quad (17b)$$

At the diaphragm a no-slip boundary condition is used for the mixture:

$$\mathbf{U} = 0 \quad (18)$$

and at the electrode surface the gas flux and mixture velocity are given by:

$$\epsilon \mathbf{u}_g = \mathbf{U} = -U_g \mathbf{n} \quad (19)$$

where the mixture and gas velocity normal to the electrode surface are set to the rate of electrochemical gas production  $U_g$  through Faraday's Law:

$$U_g = \frac{\nu'_m}{nF} j_{\perp} \quad (20)$$

where  $\nu'_m$  is the molar volume and  $n$  is the electron stoichiometric ratio for the reaction, which is 2 and 4 for hydrogen and oxygen evolution, respectively. At the anode surface a constant electrode potential is applied:

$$E_a = 0 \quad (21)$$

and at the cathode an average current density is applied so that the average current density equals the geometric current density  $j$ :

$$\frac{1}{S_c} \int_{S_c} j_{\perp} dS_c = j \quad (22)$$

The parameters for the base case simulation are given in Table 3.

## 2.4. Numerical methods

This study employs the stationary solver in COMSOL Multiphysics v6.2 with first-order discretisation for the velocity and pressure fields,

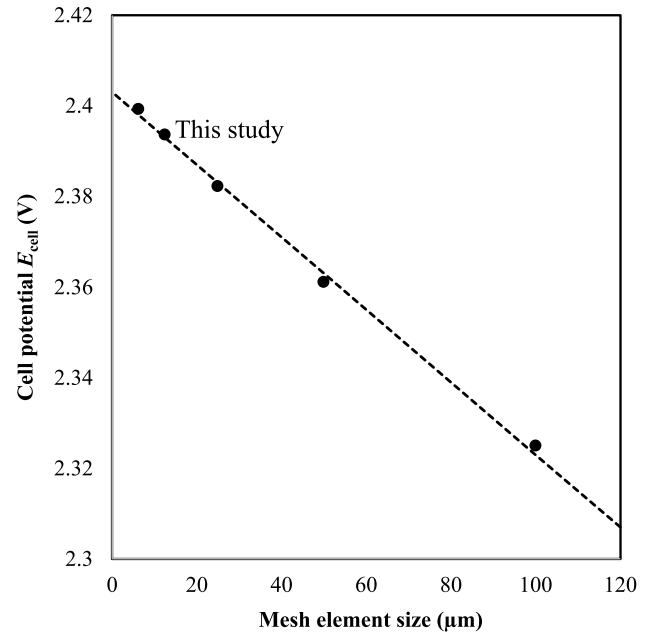


Fig. 2. Grid convergence study for the cell potential  $E_{\text{cell}}$  for meshes with different element sizes at  $j = 10^4$  A/m<sup>2</sup>. As expected for first-order discretisation, the cell potential  $E_{\text{cell}}$  converges linearly as the element size is decreased. The 12.5  $\mu\text{m}$  element size differs by only 10 mV from the extrapolated exact value for the cell potential.

the volume fraction, and the current and potential distribution. A grid convergence study with square elements ranging in size from 100  $\mu\text{m}$  to 6.25  $\mu\text{m}$  was performed. Fig. 2 shows the effect of mesh element size on the cell potential at  $j = 10^4$  A/m<sup>2</sup>. The cell potential changes linearly with decreasing mesh size, as expected for a first-order discretisation scheme. Based on this, further mesh refinement beyond an element size of 12.5  $\mu\text{m}$  is expected to result only in a change of less than 10 mV in the cell potential. An element size of 12.5  $\mu\text{m}$  was therefore chosen for this study. Over the range of element sizes used in this grid convergence study, the gas fraction distribution and velocity profiles were not significantly affected by the grid size. The dependence of the cell potential on mesh refinement is due to the large gradients in current density that occur inside the holes close to the separator. The current distribution model therefore requires a much smaller element size than the mixture model. The chosen mesh represents accurate simulation results while maintaining reasonable computational loads.

## 3. Results

### 3.1. Highest observed gas fraction

Without a solid pressure model, very high gas fractions of around 90% occur in the simulations, as shown in Fig. 3. While in theory a polydisperse bubble arrangement could exceed the maximum random packing fraction for spheres of around 64%, this is in contradiction with experimental observations of the gas fraction around electrodes, both from the back-side [9,50] and in between the electrode and membrane, while viewed through the membrane [52–54,56]. Because the flow shear inside the holes is quite low, hydrodynamic and shear-induced dispersion do not facilitate adequate bubble removal. By introducing additional bubble dispersion to the model through solid pressure, more realistic gas fractions are obtained. The shape of the curves in Fig. 3 for the different solid-pressure models of Table 3 and Eq. (8) are similar but differ in the magnitude.

The buoyancy induced by the bubbles gives rise to a liquid velocity that increases with height up to approximately 0.2 m/s. Fig. 4a shows the velocity profile in the electrolyser domain at a current

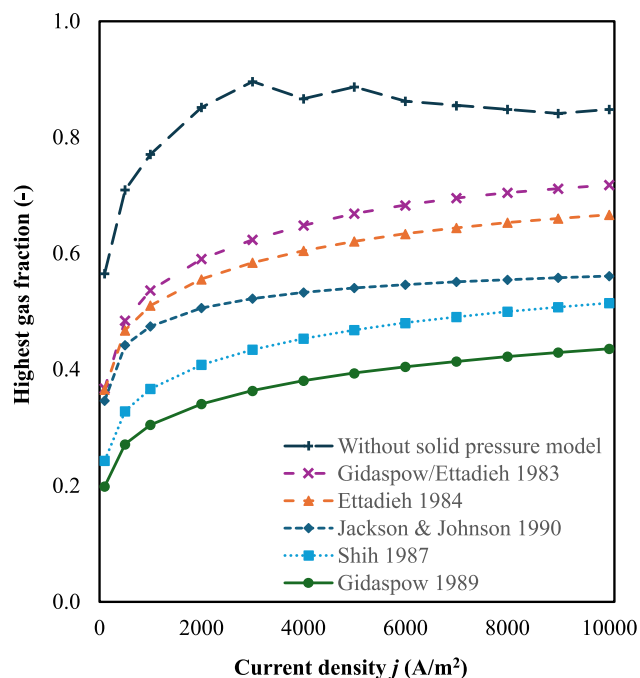


Fig. 3. The highest local gas fraction  $\varepsilon$  obtained in the simulations, against current density for various solid pressure models. For the simulation without any solid pressure model, the gas fraction is unrealistically high. See Table 3 for the used simulation parameters.

density of  $10^4$  A/m<sup>2</sup> with the Jackson and Johnson solid pressure model from Eq. (8). However, the velocity inside the holes remains limited and gas transport depends mostly on dispersion. Consequently, the highest gas fractions observed occur inside these holes, as illustrated in Figs. 4 and 5.

### 3.2. Bubble-induced resistance

Direct validation of a given gas fraction in water electrolysis is difficult, since no local measurements of the gas fraction in an operational electrolyser exist. However, the additional resistance induced by the generated bubbles is available in literature. To determine the bubble-induced losses in the simulations a bubble-free simulation case without multiphase flow model is done, in which there is no bubble effect on the conductivity of the electrolyte. The bubble-induced resistance  $R_b$  is then defined as

$$R_b = \frac{\Delta E_{\text{cell}}}{j} \quad (23)$$

where  $\Delta E_{\text{cell}}$  is the difference in cell potential between any simulation with bubble effects included and the cell potential obtained from the bubble-free simulation. This allows for a comparison of the bubble-induced resistance between the different solid pressure models and experiments. These are validated against experimental values which were obtained by measuring the increase in resistance in the first seconds after a current was applied to a cell [9], which in two independent tests gave resistances of  $1.4 \cdot 10^{-5} \Omega\text{m}^2$  and  $1.7 \cdot 10^{-5} \Omega\text{m}^2$ , respectively. The bubble-induced resistance for the various solid pressure models is shown in Fig. 6. Since the experimental values contain significant uncertainty, a range is represented by the grey shaded area. All models give results within the experimental uncertainty. The solid pressure model from Jackson & Johnson (Eq. (8)) provides both good agreement and allows significant flexibility to tune it to physically measurable parameters. The conventional literature approach without solid pressure model significantly overestimates the gas fraction, consequently resulting in a gross overestimation of the bubble-induced resistance.

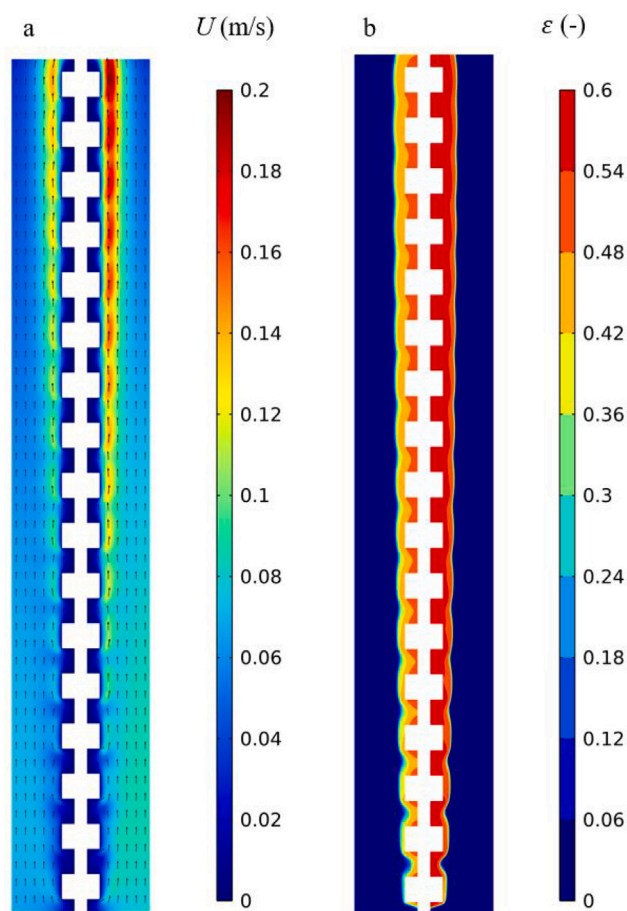


Fig. 4. (a) Mixture velocity profile and (b) gas fraction at a current density of  $10^4$  A/m<sup>2</sup>. The twice as large gas flux of the cathode on the right gives rise to higher gas fractions and larger velocities. See Table 3 for the used simulation parameters.

### 3.3. Other voltage losses in alkaline water electrolysis

Fig. 7 compares the simulated contributions to the cell potential with those determined experimentally by Haverkort and Rajaei [9]. The simulation results were obtained for a simulation using the parameters listed in Table 3. The resulting activation and ohmic overpotentials were weighted based on the current distribution to account for the local variations in current distribution, as described by Eq. (14). The equilibrium potential  $E_{\text{eq}}$  and electronic resistance  $AR$  reported in the work of Haverkort and Rajaei [9] were used as input, so match exactly. For the anode and cathode potentials, the exchange current density and Tafel slope from Haverkort and Rajaei [9] were used as input so the good agreement between the experiment and simulations is not surprising. However, the obtained ohmic resistance of approximately  $7.1 \cdot 10^{-5} \Omega/\text{m}^2$  is also in excellent agreement with the experiment, despite the fact that the resistance of the membrane contributes only  $3.67 \cdot 10^{-5} \Omega/\text{m}^2$ . The additional resistance arises due to the strong current inhomogeneity introduced by the electrode geometry, the inactive electrode front face, and the bubbles. Fig. 8 illustrates how the current lines are strongly distorted from equispaced straight lines. Since the reaction does not take place on the electrode surface facing the diaphragm [9,50] and preferentially occurs inside the holes close to the diaphragm, resistive losses mostly occur close to the diaphragm. The high gas fraction inside these holes further adds to the ohmic losses in the electrolyser. The strong current inhomogeneity introduced by the inactive electrode front and electrode geometry and the high gas fraction inside the electrode result in a significant additional resistance.

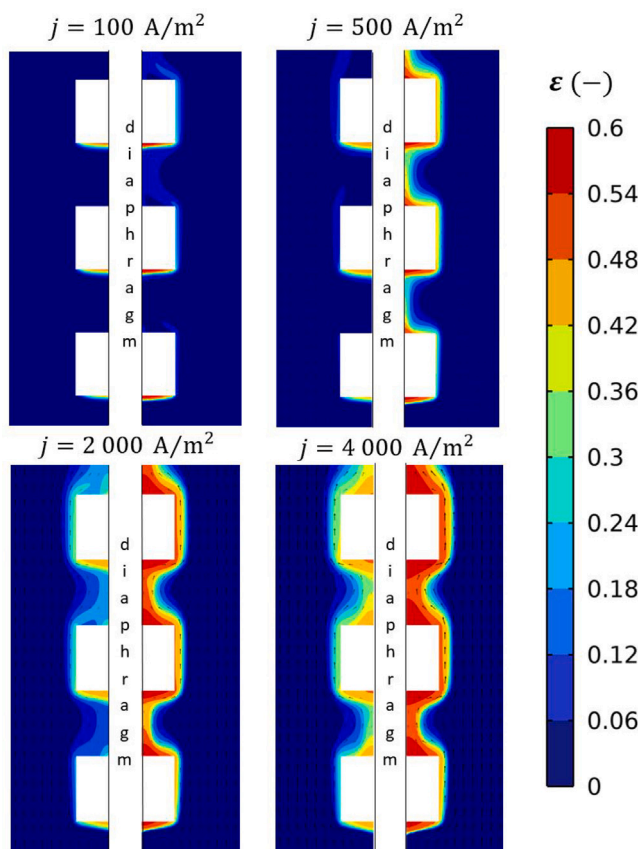


Fig. 5. Contours of the gas fraction  $\epsilon$  in increments of 0.06 around the first 6 mm in height of a simplified 2D cross-section of the electrodes and diaphragm in a zero-gap alkaline water electrolysis set-up. Results for current densities  $j$  of 100, 500, 2 000, and 4000 A/m<sup>2</sup>. The vectors show the mixture velocity field. See Table 3 for the used simulation parameters.

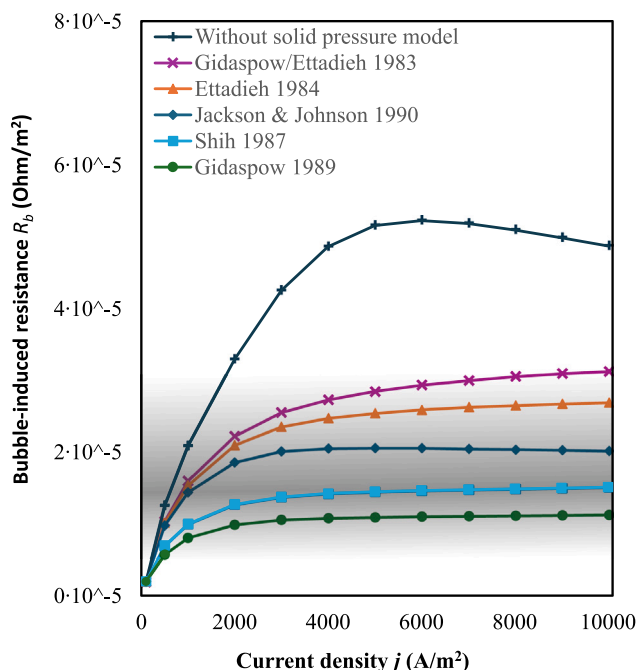


Fig. 6. The bubble-induced equivalent resistance, calculated by dividing the difference in cell potential due to bubbles by the geometrical current density, against current density for various solid pressure models. The experimentally determined bubble-induced resistance [9] contains significant uncertainty, and as such a range is represented by the grey shaded area. See Table 3 for the simulation parameters used.

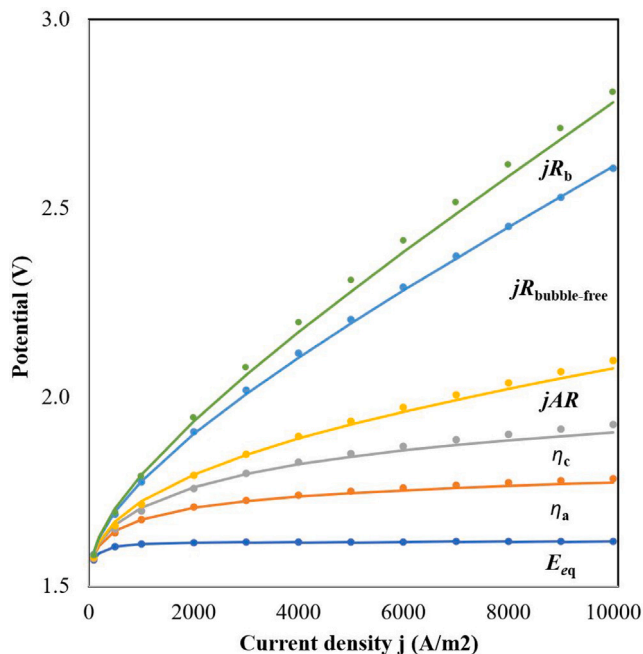


Fig. 7. The cumulative effects of the equilibrium potential  $E_{eq}$ , anodic and cathodic activation overpotentials  $\eta_a$  and  $\eta_c$ , electrode ohmic losses  $AR_j$ , bubble-free ohmic losses  $jR_{bubble-free}$ , and bubble-induced ohmic losses  $jR_b$ . Solid lines show model values based on experimental fits using  $R_{bubble-free} = 5.35 \times 10^{-5} \Omega m^2$  and  $R_b = 1.68 \times 10^{-5} \Omega m^2$  from Haverkort and Rajaei [9]. The discrete data points represent the corresponding potentials resulting from the simulations in the present study. See Table 3 for the used simulation parameters.

This strong difference between the diaphragm resistance and the actual resistance was previously investigated by de Groot and Vreman [4] by assuming a chosen value for a homogeneous gas fraction. Here we instead calculate the gas fraction by coupling the local gas production rate to the current density at the electrode, and further describe the bubble transport around the electrodes with an extended multiphase flow model. This presents a crucial next step forward towards a comprehensive model of the relevant processes in and around gas-evolving electrodes.

#### 4. Conclusions

Conventional bubble dispersion models used in flat-plate alkaline water electrolysis simulations are shown to be inadequate for electrode-resolved simulations. Without additional measures unrealistically high gas fractions are obtained, even at current densities much lower than typically used in alkaline water electrolyzers. As a result, the resistance due to bubbles is strongly overestimated.

We propose to include a solid pressure model, in analogy with simulations of dense granular flows. The associated force effectively prevents nonphysically high gas fractions by increasing the degree of bubble dispersion as the gas fraction increases. The used 2D representation of a zero-gap configuration matches experimental results for activation overpotentials and ohmic losses well, and most importantly can accurately predict the bubble-induced ohmic losses. All tested solid-pressure models give relatively similar results, with the Jackson & Johnson model [70] showing the best agreement with the experimental data. The scope current work is limited to laminar flow conditions. While only limited velocities occur inside the holes of the electrode, the effect of turbulence on bubble dispersion in the electrode holes remains

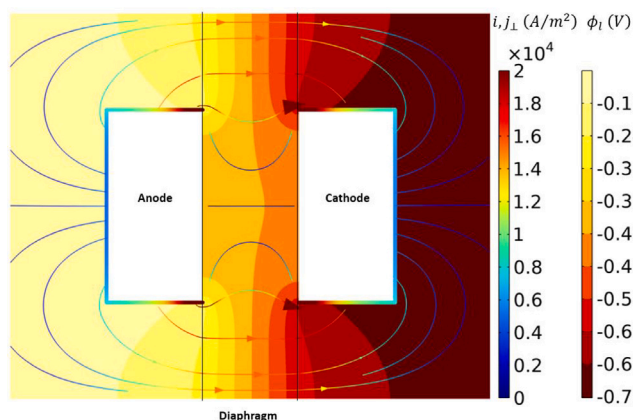


**Fig. 8.** Contours of the electrolyte potential  $\phi_l$  around the 2D cross-section of an alkaline water electrolyser in zero-gap configuration at a current density of  $j = 10^4$  A/m<sup>2</sup>. The surface current density  $j_{\perp}$  is given at the electrodes and the local electrolyte current density  $i$  is given by the streamline plot. See Table 3 for the used simulation parameters.

a subject of further research.

The proposed methodology includes the interaction between local current and gas fraction distributions. This allows, for the first time, for predictive modeling of the local overpotentials in alkaline water electrolysis. The improved understanding given by this model of the interaction between current distribution and bubbles signifies a next step in the design and optimisation of gas-evolving electrodes.

#### CRediT authorship contribution statement

**W.L. van der Does:** Writing – review & editing, Writing – original draft, Visualization, Validation, Project administration, Methodology, Formal analysis, Conceptualization. **N. Valle:** Writing – review & editing, Supervision, Methodology. **J.W. Haverkort:** Writing – review & editing, Validation, Supervision, Methodology, Funding acquisition, Conceptualization.

#### Declaration of competing interest

The authors declare that they have no known competing financial interests or personal relationships that could have appeared to influence the work reported in this paper.

#### References

[1] Götz M, Lefebvre J, Mörs F, Koch AM, Graf F, Bajohr S, Reimert R, Kolb T. Renewable power-to-gas: A technological and economic review. *Renew Energy* 2016;85:1371–90. <http://dx.doi.org/10.1016/j.renene.2015.07.066>.

[2] Phillips R, Edwards A, Rome B, Jones DR, Dunnill CW. Minimising the ohmic resistance of an alkaline electrolysis cell through effective cell design. *Int J Hydrog Energy* 2017;42(38):23986–94.

[3] Pletcher D, Li X. Prospects for alkaline zero gap water electrolyzers for hydrogen production. *Int J Hydrog Energy* 2011;36(23):15089–104.

[4] de Groot MT, Vreman AW. Ohmic resistance in zero gap alkaline electrolysis with a zircon diaphragm. *Electrochim Acta* 2021;369. <http://dx.doi.org/10.1016/j.electacta.2020.137684>.

[5] Smolinka T, Bergmann H, Garche J, Kusnezoff M. The history of water electrolysis from its beginnings to the present. In: *Electrochemical power sources: fundamentals, systems, and applications*. Elsevier; 2022, p. 83–164.

[6] Schalenbach M, Tjarks G, Carmo M, Lueke W, Mueller M, Stolten D. Acidic or alkaline? Towards a new perspective on the efficiency of water electrolysis. *J Electrochem Soc* 2016;163(11):F3197.

[7] Pletcher D, Li X, Wang S. A comparison of cathodes for zero gap alkaline water electrolyzers for hydrogen production. *Int J Hydrog Energy* 2012;37(9):7429–35.

[8] Kraglund MR, Aili D, Jankova K, Christensen E, Li Q, Jensen JO. Zero-gap alkaline water electrolysis using ion-solvating polymer electrolyte membranes at reduced KOH concentrations. *J Electrochem Soc* 2016;163(11):F3125.

[9] Haverkort JW, Rajaei H. Voltage losses in zero-gap alkaline water electrolysis. *J Power Sources* 2021;497. <http://dx.doi.org/10.1016/j.jpowsour.2021.229864>.

[10] Barros LRG, Kraakman JT, Sebregts C, van der Schaaf J, de Groot MT. Impact of an electrode-diaphragm gap on diffusive hydrogen crossover in alkaline water electrolysis. *Int J Hydrog Energy* 2024;49:886–96.

[11] Schröder V, Holtappels K. Explosion characteristics of hydrogen-air and hydrogen-oxygen mixtures at elevated pressures. 2005.

[12] Nagai N, Takeuchi M, Kimura T, Oka T. Existence of optimum space between electrodes on hydrogen production by water electrolysis. *Int J Hydrog Energy* 2003;28:35–41. URL: [www.elsevier.com/locate/ijhydene](http://www.elsevier.com/locate/ijhydene).

[13] Hine F, Murakami K. Bubble effects on the terminal with perforated voltage of a vertical cell electrodes. *J Electrochem Soc* 1981;128:64.

[14] Kreysa G, Kuhn M. Modelling of gas evolving electrolysis cells. I. The gas voidage problem. *J Appl Electrochem* 1985;15(4):517–26.

[15] Elsner C, Coeuret F. Potential distribution along gas evolving electrodes\*. *J Appl Electrochem* 1985;15:567–74.

[16] Boissonneau P, Byrne P. An experimental investigation of bubble-induced free convection in a small electrochemical cell. *J Appl Electrochem* 2000;30:767–75.

[17] Hine F, Murakami K. Bubble effects on the solution IR drop in a vertical electrolyzer under free and forced convection. *J Electrochem Soc* 1980;127(2):292.

[18] Bisang J. Current distribution in a gas-evolving electrochemical reactor with an expanded metal electrode. *J Appl Electrochem* 1992;22(6):585–7.

[19] Janssen L, Visser G. Behaviour of a tall vertical gas-evolving cell part II: Distribution of current. *J Appl Electrochem* 1991;21(9):753–9.

[20] Coenen E, Janssen L. Voidage of bulk solution in a tall vertical gasevolving cell. *J Appl Electrochem* 1997;27:1143–8.

[21] Kuhn M, Kreysa G. Modelling of gas-evolving electrolysis cells. II. Investigation of the flow field around gas-evolving electrodes. *J Appl Electrochem* 1989;19(5):677–82.

[22] Leuaa P, Kraglund MR, Chatzichristodoulou C. Decoupling of reaction overpotentials and ionic transport losses within 3D porous electrodes in zero-gap alkaline electrolysis cells. *Electrochim Acta* 2023;470:143306.

[23] Lee HI, Cho H-S, Kim M, Lee JH, Lee C, Lee S, Kim S-K, Kim C-H, Yi KB, Cho W-C. The structural effect of electrode mesh on hydrogen evolution reaction performance for alkaline water electrolysis. *Front Chem* 2021;9.

[24] Nishiki Y, Aoki K, Tokuda K, Matsuda H. Primary current distribution in a two-dimensional model cell composed of an electrode with an open part. *J Appl Electrochem* 1984;14:653–61.

[25] Nishiki Y, Aoki K, Tokuda K, Matsuda H. Secondary current distribution in a two-dimensional model cell composed of an electrode with an open part. *J Appl Electrochem* 1986;16(2):291–303.

[26] Nishiki Y. Current distribution in a two-dimensional narrow gap cell composed of a gas evolving electrode with an open part. *J Appl Electrochem* 1987;17:67–76.

[27] Nishiki Y, Nakamatsu S, Aoki K, Tokuda K. Estimation of optimum anode geometry in chlor-alkali membrane cells. *J Appl Electrochem* 1989;19:90–4.

[28] Dahlkild AA. Modelling the two-phase flow and current distribution along a vertical gas-evolving electrode. *J Fluid Mech* 2001;428:249–72.

[29] Jupudi RS, Zhang H, Zappi G, Bourgeois R. Modeling bubble flow and current density distribution in an alkaline electrolysis cell. *J Comput Multiph Flows* 2009;1(4):341–7.

[30] Mat MD, Aldas K. Application of a two-phase flow model for natural convection in an electrochemical cell. *Int J Hydrog Energy* 2005;30(4):411–20.

[31] Mat MD, Kaplan Y, Ibrahimoglu B, Veziroglu N, Alibeyli R, Kuliyeve S. A mathematical model for hydrogen evolution in an electrochemical cell and experimental validation. *Gas* 2006;2:4e.

[32] Aldas K, Pehlivanoglu N, Mat MD. Numerical and experimental investigation of two-phase flow in an electrochemical cell. *Int J Hydrog Energy* 2008;33:3668–75. <http://dx.doi.org/10.1016/j.ijhydene.2008.04.047>.

[33] Lee J, Alam A, Park C, Yoon S, Ju H. Modeling of gas evolution processes in porous electrodes of zero-gap alkaline water electrolysis cells. *Fuel* 2022;315:123273.

[34] Yang W, Sun L, Tang J, Mo Z, Liu H, Du M, Bao J. Multiphase fluid dynamics and mass transport modeling in a porous electrode toward hydrogen evolution reaction. *Ind Eng Chem Res* 2022;61(23):8323–32.

[35] Duan X, Xiao J, Peng X, Feng S, Wang S, Wen J. Multi-objective optimization of water electrolysis based on coupling model of electrochemistry and multiphase flow. *J Environ Chem Eng* 2023;11(6):110985.

[36] Duan X, Zhou A, Liu Q, Xiao J, Wen J, Wang S. Numerical simulation and structural optimization of electrolyzer based on the coupled model of electrochemical and multiphase flow. *Int J Hydrog Energy* 2024;49:604–15.

[37] Wedin R, Dahlkild AA. On the transport of small bubbles under developing channel flow in a buoyant gas-evolving electrochemical cell. *Ind Eng Chem Res* 2001;40:5228–33. <http://dx.doi.org/10.1021/ie001073u>.

[38] Schillings J, Doche O, Deseure J. Modeling of electrochemically generated bubbly flow under buoyancy-driven and forced convection. *Int J Heat Mass Transfer* 2015;58:292–9. <http://dx.doi.org/10.1016/j.ijheatmasstransfer.2015.01.121>.

[39] Schillings J, Doche O, Retamales MT, Bauer F, Deseure J, Tardu S. Four-way coupled Eulerian–Lagrangian direct numerical simulations in a vertical laminar channel flow. *Int J Multiph Flow* 2017;89:92–107.

- [40] Liu C-L, Sun Z, Lu G-M, Yu J-G. Hydrodynamic characteristics of the two-phase flow field at gas-evolving electrodes: Numerical and experimental studies. *R Soc Open Sci* 2018;5(5):171255.
- [41] Bideau DL, Mandin P, Benbouzid M, Kim M, Sellier M, Ganci F, Inguanta R. Eulerian two-fluid model of alkaline water electrolysis for hydrogen production. *Energies* 2020;13. <http://dx.doi.org/10.3390/en13133394>.
- [42] Zarghami A, Deen NG, Vreman AW. CFD modeling of multiphase flow in an alkaline water electrolyzer. *Chem Eng Sci* 2020;227. <http://dx.doi.org/10.1016/j.ces.2020.115926>.
- [43] Dreoni M, Balduzzi F, Ferrara G, Bianchini A. Accuracy assessment of the Eulerian two-phase model for the CFD simulation of gas bubbles dynamics in alkaline electrolyzers. In: *Journal of physics: conference series*. Vol. 2385, IOP Publishing; 2022, 012040.
- [44] Wosiak G, da Silva J, Sena SS, de Andrade RN, Pereira E. CFD simulation and experimental comparison of bubble-induced convection during electrochemical water splitting. *Chem Eng J* 2022;433:133194.
- [45] Abdelouahed L, Hreiz R, Poncin S, Valentin G, Lapique F. Hydrodynamics of gas bubbles in the gap of lantern blade electrodes without forced flow of electrolyte: Experiments and CFD modelling. *Chem Eng Sci* 2014;111:255–65.
- [46] Mandin P, Hamburger J, Bessou S, Picard G. Modelling and calculation of the current density distribution evolution at vertical gas-evolving electrodes. *Electrochim Acta* 2005;51(6):1140–56.
- [47] Alexiadis A, Dudukovic M, Ramachandran P, Cornell A. On the stability of the flow in multi-channel electrochemical systems. *J Appl Electrochem* 2012;42:679–87.
- [48] Hreiz R, Abdelouahed L, Fuenfschilling D, Lapique F. Electrogenated bubbles induced convection in narrow vertical cells: PIV measurements and Euler–Lagrange CFD simulation. *Chem Eng Sci* 2015;134:138–52.
- [49] Hess S, Zhang S, Kadyk T, Lehnert W, Eikerling M, Beale SB. Numerical two-phase simulations of alkaline water electrolyzers. *ECS Trans* 2023;112(4):419.
- [50] Kienzlen V, Haaf D, Schnurnberger W. Location of hydrogen gas evolution on perforated plate electrodes in zero gap cells. *Int J Hydrog Energy* 1994;19:729–32.
- [51] Sillen C, Barendrecht E, Janssen L, Van Stralen S. Gas bubble behaviour during water electrolysis. In: *Hydrogen as an energy vector: proceedings of the international seminar, Held in Brussels, 12–14 February 1980*. Springer; 1980, p. 328–48.
- [52] Lentjes D. Effect of bubble behaviour on the performance of a zero-gap chlor-alkali electrolyzer. 2022.
- [53] Craye E. Bubble quantification: in the near electrode region in alkaline water electrolysis. 2023.
- [54] Qiu H, Obata K, Tsuburaya K, Nishimoto T, Nagato K, Takanabe K. Impact of gas bubble slug on high-frequency resistance and cell voltage in water electrolysis device. *J Power Sources* 2024;611:234765.
- [55] Barros RLG, Kelleners MH, van Bommel L, van der Leege TV, van der Schaaf J, de Groot MT. Elucidating the increased ohmic resistances in zero-gap alkaline water electrolysis. *Electrochim Acta* 2024;145161.
- [56] Haverkort JW, Craye EJB, Aghdam AS. The optimal electrode hole size, shape, and open-area fraction in zero gap alkaline water electrolysis : a combined electrochemical and optical approach. *Journal* 2025.
- [57] Janssen L, Sillen C, Barendrecht E, Van Stralen S. Bubble behaviour during oxygen and hydrogen evolution at transparent electrodes in KOH solution. *Electrochim Acta* 1984;29(5):633–42.
- [58] Duignan TT. The surface potential explains ion specific bubble coalescence inhibition. *J Colloid Interface Sci* 2021;600:338–43.
- [59] Ishii M, Hibiki T. *Thermo-fluid dynamics of two-phase flow*. Springer Science & Business Media; 2011.
- [60] Manninen M, Taivassalo V, Kallio S. On the mixture model for multiphase flow. 1996.
- [61] Ishii M, Zuber N. Drag coefficient and relative velocity in bubbly, droplet or particulate flows. *AIChE J* 1979;25(5):843–55.
- [62] Clift R, Grace JR, Weber ME. *Bubbles, drops, and particles*. Courier Corporation; 2013.
- [63] Nicolai H, Herzhaft B, Hinch E, Oger L, Guazzelli E. Particle velocity fluctuations and hydrodynamic self-diffusion of sedimenting non-Brownian spheres. *Phys Fluids* 1995;7(1):12–23.
- [64] Rajora A, Haverkort JW. An analytical multiphase flow model for parallel plate electrolyzers. *Chem Eng Sci* 2022;260. <http://dx.doi.org/10.1016/j.ces.2022.117823>.
- [65] Leighton D, Acrivos A. Measurement of shear-induced self-diffusion in concentrated suspensions of spheres. *J Fluid Mech* 1987;177:109–31.
- [66] Enwald H, Peirano E, Almstedt A-E. Eulerian two-phase flow theory applied to fluidization. *Int J Multiph Flow* 1996;22:21–66.
- [67] Josserand C, Lagrée P-Y, Lhuillier D. Granular pressure and the thickness of a layer jamming on a rough incline. *Europhys Lett* 2005;73(3):363.
- [68] Massoudi M, Rajagopal K, Ekman J, Mathur M. Remarks on the modeling of fluidized systems. *AIChE J* 1992;38(3):471–2.
- [69] Valle N, Haverkort J. Self-similar solution for laminar bubbly flow evolving from a vertical plate. *J Fluid Mech* 2024.
- [70] Johnson PC, Nott P, Jackson R. Frictional–collisional equations of motion for particulate flows and their application to chutes. *J Fluid Mech* 1990;210:501–35.
- [71] Gidaspow D, Ettehadieh B. Fluidization in two-dimensional beds with a jet. 2. Hydrodynamic modeling. *Ind Eng Chem Fundam* 1983;22(2):193–201.
- [72] Ettehadieh B, Gidaspow D, Lyczkowski R. Hydrodynamics of fluidization in a semicircular bed with a jet. *AIChE J* 1984;30(4):529–36.
- [73] Shih Y, Gidaspow D, Wasan D. Hydrodynamics of sedimentation of multisized particles. *Powder Technol* 1987;50(3):201–15.
- [74] Gidaspow D, Shih Y-T, Bouillard J, Wasan D. Hydrodynamics of a lamella electrosettler. *AIChE J* 1989;35(5):714–24.
- [75] Haverkort J. *Electrolysers, fuel cells and batteries: analytical modelling*. TU Delft OPEN; 2024.
- [76] Rodríguez J, Palmas S, Sánchez-Molina M, Amores E, Mais L, Campana R. Simple and precise approach for determination of ohmic contribution of diaphragms in alkaline water electrolysis. *Membranes* 2019;9(10):129.
- [77] Brangeon B, Joubert P, Bastide A. Influence of the dynamic boundary conditions on natural convection in an asymmetrically heated channel. *Int J Therm Sci* 2015;95:64–72.
- [78] Sun H, Li R, Chénier E, Lauriat G. On the modeling of aiding mixed convection in vertical channels. *Heat Mass Transf* 2012;48(7):1125–34.
- [79] Desrayaud G, Chénier E, Joulin A, Bastide A, Brangeon B, Caltagirone J, Cherif Y, Eymard R, Garnier C, Giroux-Julien S, et al. Benchmark solutions for natural convection flows in vertical channels submitted to different open boundary conditions. *Int J Therm Sci* 2013;72:18–33.
- [80] Habibi P, Rahbari A, Blazquez S, Vega C, Dey P, Vlught TJ, Moulton OA. A new force field for OH<sup>-</sup> for computing thermodynamic and transport properties of H<sub>2</sub> and O<sub>2</sub> in aqueous NaOH and KOH solutions. *J Phys Chem B* 2022;126(45):9376–87.